PHYSICAL REVIEW B **76**, 174301 (2007)

Acoustic phonon nanowave devices based on aperiodic multilayers: Experiments and theory

N. D. Lanzillotti-Kimura,[1,*] A. Fainstein,[1,†] B. Jusserand,[2] A. Lemaître,[3] O. Mauguin,[3] and L. Largeau[3]
[1]*Centro Atómico Bariloche and Instituto Balseiro, CNEA, 8400 San Carlos de Bariloche, Río Negro, Argentina*
[2]*Institut des NanoSciences de Paris, UMR 7588 CNRS-Université Pierre et Marie Curie, 75015 Paris, France*
[3]*Laboratoire de Photonique et de Nanostructures, CNRS, 91460 Marcoussis, France*
(Received 26 June 2007; published 13 November 2007)

We describe multilayer acoustic nanowave devices based on aperiodic stacks of GaAs and AlAs layers and achievable with standard molecular beam epitaxy (MBE) technology. These nanostructures were designed to display optimized acoustic reflectivity curves in the terahertz range. We discuss the use of different techniques for the design, optimization, and characterization of such acoustic phonon devices. Three optimized acoustic phonon devices were grown by MBE and characterized structurally by x-ray diffraction and photoluminescence: a broadband mirror, a color filter, and an edge filter. The acoustic phonon spectra were studied by Raman scattering in forward and backscattering geometries. We contrast the experimental results with simulations of the Raman spectra using a photoelastic model. We show that Raman spectroscopy provides a powerful tool to acoustically characterize complex aperiodic devices.

DOI: 10.1103/PhysRevB.76.174301 PACS number(s): 63.22.+m, 68.60.Bs, 78.30.Fs, 78.67.Pt

I. INTRODUCTION

Acoustic phonons play a central role in the thermal energy transport and recombination processes, and limit the electrical conductivity in technologically important semiconductors. In addition, they can be used as sensitive nanoscopic probes of thermodynamic phases, piezoelectric fields, and electronic states, and for nanostructure characterization. Phonon engineering,[1,2] i.e., the control and manipulation of acoustic reflectivity, phonon group velocity, density of states, polarization, etc., has implications in the control of sound, light, and charge at high frequencies in the nanoscale.

A periodic stack of two materials with contrasting acoustic impedances reflects sound.[3] The first $k=0$ folded phonon minigap in a superlattice (SL) is maximum, with the layer thickness (d) ratio given by $d_1/v_1=d_2/3v_2$. The width of the stop band and the reflectivity of such a phonon mirror are determined by the acoustic impedance mismatch $Z=\rho_1 v_1/\rho_2 v_2$ and the number of SL periods.[4–6] Periodic phonon mirrors represent the simplest example of a phonon device. The effects of inhomogeneities on the propagation of acoustic waves in periodic, elastic multilayered structures have been extensively studied.[5,7–12] Particularly, the presence of a cavity layer in a regular SL has been studied both theoretically[8,9] and experimentally by Raman scattering[5,9] and picosecond acoustics.[10] More complex nonperiodic devices like Bloch resonators[12] based on cavity structures have theoretically been studied in the terahertz range, and demonstrated in the domain of acoustics.[13]

Another kind of nonperiodic multilayers is represented by the quasiperiodic (Fibonacci), Thue-Morse and random SLs.[14] These systems have been studied theoretically[15] and experimentally by x-ray diffraction,[16–18] photoluminescence,[19] and Raman scattering.[14,17,18,20]

Recently, in the kilohertz domain, a series of acoustic devices based both on two-dimensional and three-dimensional phononic crystals were designed and studied, e.g., mirrors,[21,22] phononic lenses,[23] waveguides,[24] and demultiplexers,[25,26] to name a few. However, the implementations of their equivalent in the terahertz range posses additional and specific challenges. In this work, we address the problem of designing, growing, and characterizing optimized nanowave devices with tailored acoustic reflectivities for the terahertz range based on nonperiodic one-dimensional multilayers.

Optimized acoustic phonon filters and mirrors in the terahertz range,[1] i.e., devices which have a specific spectral reflectivity, have potential applications in picoseconds acoustics, coherent phonon generation, phonon optics, nanostructure characterization, and in optoelectronic devices where simple periodic structures do not satisfy the required acoustic response. Optimized phonon filters are the acoustic equivalent to the already developed multilayer optical thin-film filters.[27] These phononic devices, in the terahertz range, are designed to control "sound" wavelengths of a few nanometers. The required variations in the thicknesses are thus of the order of a few monolayers, lying in the practical limit of construction of multilayered structures.

The strong development of different growing techniques such as molecular beam epitaxy (MBE) provides the high standard requirements for the development of phonon mirrors, filters, and other acoustic analogs of classical optical elements in semiconductor and in oxide systems.[6,28]

Phononics has profited and obtained inspiration from previous work in the domain of photonics. Though a clear parallel exists between optics and phononics, there are some issues that are specific to phononics in the terahertz range and that pose exigent challenges for its implementation in technology. An important difference between optics and hyperacoustics in the terahertz range is the characterization of samples. In fact, the access to spectral and time domain probes with sufficient resolution to test hyperacoustic multilayered devices represents today an active research field.[1,10,11] For example, the lack of monochromatic sources and detectors is one expression of this limitation.

We focus our work on artificial GaAs/AlAs nonperiodic multilayers. We address the problem of obtaining acoustic filters and mirrors which have specific spectral reflectivities by using multivariable optimization techniques, and we dis-

©2007 The American Physical Society

cuss different strategies for their structural and acoustic characterizations.

In a previous short communication, we presented preliminary results on the design and characterization using Raman scattering of two phononic filters.[1] In this paper, we discuss in more detail the optimization procedure and we present a full set of characterization results and the complete analysis of complex nonperiodic multilayers through Raman scattering in different geometries. Three optimized phonon devices were grown by MBE: a broadband mirror, a color filter, and an edge filter. These devices were structurally characterized through x-ray diffraction and photoluminescence, and acoustically through high resolution Raman scattering. Finally, we contrast the experimental results with simulations. The paper is organized as follows. In Sec. II, we present the design and optimization techniques and a series of examples of nonperiodic acoustic phonon devices. Structural characterization of the three grown devices through x-ray diffraction and photoluminescence is discussed in Sec. III. Section IV presents the motivation and a theoretical analysis on the use of Raman scattering as a characterization tool for phononic devices and its use as input for an inverse engineering process. Section V presents the results on high resolution Raman scattering experiments and simulations. Finally, the discussion and conclusions are presented in Sec. VI.

II. DESIGN AND OPTIMIZATION OF PHONONIC DEVICES

In this section, we present the results on the design and optimization of acoustic phonon devices in the terahertz range that have an equivalent in the field of optics. Devices such as broadband mirrors, edge filters, notch filters, and color filters are discussed in this section to illustrate different criteria to design complex phononic structures.

Different optimized acoustic devices can be conceived, depending on the nature of the application they would be implemented in. A device that will surely be required if only broadband sources are available is the broadband mirror. That is, mirrors with a high-reflectivity stop band much wider than that of periodic phonon Bragg mirrors. It turns out that a superstructure with GaAs/AlAs layers that decrease in a fixed amount as a function of the period number (0.3% in the present case) leads to reflectivity stop bands much larger than those of periodic structures with the same acoustic impedance mismatch.[29] From now on, all the reflectivity calculations are made using a transfer matrix method.[12,30] It is worthwhile to underline that acoustic attenuation effects are not addressed in this paper. We present in Fig. 1 the calculated phonon reflectivity and corresponding layer thicknesses for a 160 layer GaAs/AlAs broadband phonon mirror. For comparison, the reflectivity and layer thicknesses of the periodic mirror are also shown. Note that the reflectivity is above 97% throughout the whole spectral region that extends between 18.5 and 23.5 cm^{-1}, a stop band more than five times broader than that of the corresponding GaAs/AlAs periodic structure.

The reflectivity curve of the broadband mirror is a relatively simple one, and the designing parameters are easily identified: number of layers, materials, and thickness gradient. Notwithstanding the relevance and adaptability of this device, more complex acoustic filters will be required in phononic applications, e.g., edge, notch, and color filters, to name the most common ones. The conception of these devices cannot be achieved by just piling up periodic structures or by introducing a gradient in the thicknesses as in the case of the broadband mirror. The design of these aperiodic devices requires solving an inverse problem.

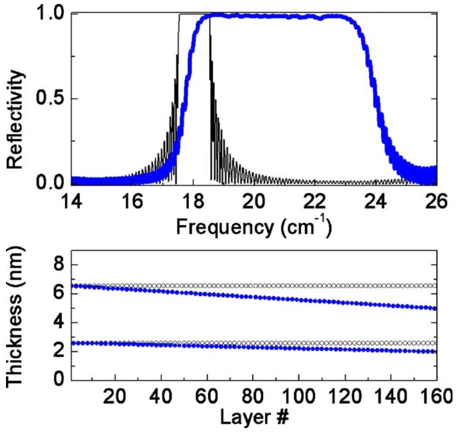

FIG. 1. (Color online) (Top) Calculated acoustic reflectivity for a broadband mirror made with 160 GaAs/AlAs layers (thick line). For comparison purposes, the reflectivity of a periodic array is also shown (thin line). (Bottom) Layer thicknesses corresponding to the optimized broadband mirror (full dots) and the corresponding periodic phonon mirror (empty circles).

An inverse problem consists of the reconstruction or optimal design of a set of parameters in a system to achieve a desired state. In our case, the set of parameters is given by the distribution of the layer thicknesses in a nonperiodic multilayer, and the goal is to achieve a specific acoustic reflectivity. To address the inverse problem, it is a requirement to know an efficient way to solve the associated direct problem, which consists, in our case, in the simulation of the acoustic reflectivity when the thickness distribution is known. To calculate the acoustical reflectivity, as already stated, we used a transfer matrix method.[12,30] As multidimensional optimization tool, we used the Nelder and Mead (NM) downhill simplex routine.[31]

The NM method is based on geometrical transformations of a simplex, a nonplanar figure which has $N+1$ vertices in an N-dimensional space.[31–34] The coordinates of each vertex of the simplex represent a possible solution of the inverse problem, and in this case, they are the layer thicknesses of a potential nonperiodic solution.[1] The full set of coordinates of the simplex is represented by an $(N+1)\times N$ matrix, where each component is a thickness value (in nanometers and without taking into account any correspondence with the number of layers). Each vertex has an associated value of objective function, given by the standard Euclidean distance between the acoustic reflectivity of the candidate structure and the target acoustic reflectivity. The algorithm operates by moving an n-dimensional simplex through R^n, replacing the current worst vertex (which has the highest objective func-

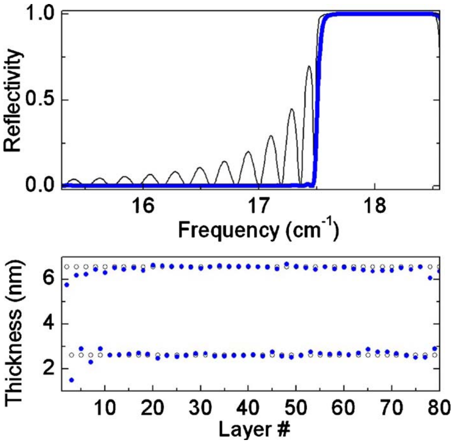

FIG. 2. (Color online) (Top) Calculated acoustic reflectivity for an edge filter made with 80 GaAs/AlAs layers (thick line). For comparison purposes, the reflectivity of a periodic array is also shown (thin line). (Bottom) Layer thicknesses corresponding to the optimized edge filter (full dots) and the corresponding periodic phonon mirror (empty circles).

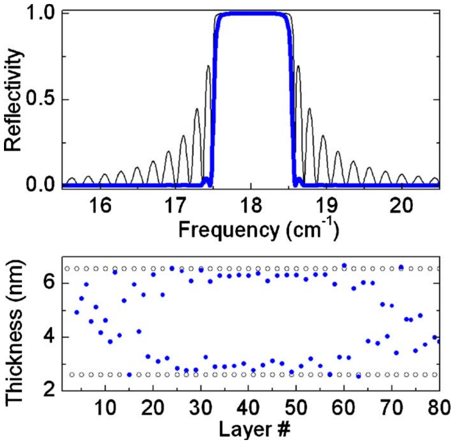

FIG. 3. (Color online) (Top) Calculated acoustic reflectivity for an optimized notch filter made with 80 GaAs/AlAs layers (thick line). For comparison purposes, the reflectivity of a periodic ($\lambda/4, 3\lambda/4$) array is also shown (thin line). (Bottom) Layer thicknesses corresponding to the optimized notch filter (full dots) and the periodic phonon mirror used as seed (empty circles).

tion value) at each iteration, and changing the shape and/or the size of the figure. The process continues until an acceptable solution has been reached or until the algorithm has converged.[31] At each iteration, the algorithm reflects, stretches, and/or shrinks the simplex by applying algebraic operators between the rows of the matrix. All the vertex coordinates in the initial simplex are taken as random thicknesses between 0 and 10 nm. When indicated, a seed is used in the initial simplex. That is, the coordinates of a vertex are specifically chosen, and not randomly like the rest of the vertices. The problem we address is characterized by having several feasible solutions, along with multiple local minima. Both the feasible solutions and local minima can be defined as continuous regions in the parameter space that satisfy the following convergence criteria for all the vertices X of the simplex:

$$f(X_i) - f(X_j) < K, \tag{1}$$

where $f(X)$ is the objective function evaluated in X, and K is a constant real value. To consider a structure as a feasible solution, it must satisfy an additional condition:

$$f(X) < C, \tag{2}$$

where C is again a real value.

Using the NM optimization scheme, we focus on the design of an edge filter. An edge filter is a device that has a high transmission below (above) a well defined energy edge and a high reflectivity above (below) it. In Fig. 2, we show the calculated reflectivity for an optimized edge filter. From now on, we will call this device basic edge filter to distinguish it from a more complex edge filter that we will analyze later in this section. The acoustic reflectivity of a periodic superlattice is shown in the same figure for comparison purposes. Note that in the low energy region, the reflectivity practically reaches zero in all the optimized range, and that in the high energy region, the stop band is the same as in the case of a periodic superlattice. The optimization was performed using a periodic 80 layer GaAs/AlAs 6.56/2.61 nm SL seed to obtain a basic edge filter F$_A$. F$_A$ was conceived to have a high transmittance from 15.30 to 17.46 cm^{-1} and high reflectivity in the 17.60–18.54 cm^{-1} region. The value reached for the constant C was 1.21×10^{-5}. Outside the optimization region (not shown in the figure), the acoustic reflectivity displays interference oscillations that may need to be taken into account when using these optimized devices. In the lower panel of Fig. 2, the thickness distribution of the optimized edge filter (full dots) and the corresponding periodic structure (empty circles) are shown. Note that the attenuation of the low energy oscillations requires only small variations in the thicknesses of the periodic SL, variations that are concentrated mostly at the edges of the device.

The second optimized sample is a notch filter. A notch filter is a device which blocks a narrow band of frequencies and passes all frequencies above and below the band. The target reflectivity can be thought of as that of a periodic SL without the characteristic oscillations in both sides of the stop band. This led us to consider the use of a periodic SL as seed, as in the previous case. The spectral position and width of the high-reflectivity region are then determined by the stop band of this SL. Figure 3 shows the calculated reflectivity for the optimized notch filter. The acoustic reflectivity of the seed is also shown. In the lower panel of Fig. 3, the thicknesses of the corresponding layers, compared to those of the periodic GaAs/AlAs 5.56/2.61 nm phonon mirror (optimized $3\lambda/4-\lambda/4$ ratio), are also shown. It can be observed, again, that the main changes with respect to the periodic array occur at the beginning and at the end of the device. However, in comparison with the edge filter, the modifications are more important, and extend throughout the whole structure. With the exception of two strongly reduced oscillations that remain at both sides of the high-reflectivity region, all oscillations are almost completely suppressed. The reflectivity within the forbidden region is not altered,

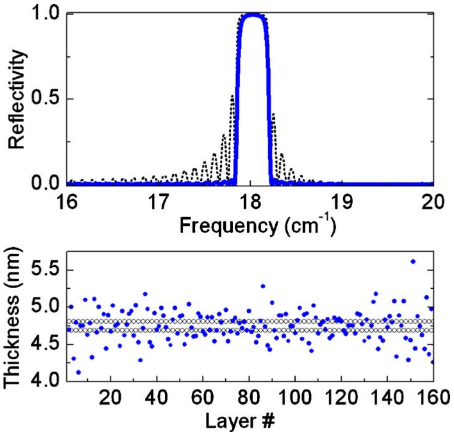

FIG. 4. (Color online) (Top) Calculated acoustic reflectivity for an optimized notch filter made with 160 GaAs/AlAs layers (thick line). For comparison purposes, the reflectivity of a periodic (0.55λ,0.45λ) array is also shown (thin line). (Bottom) Layer thicknesses corresponding to the optimized notch filter (full dots) and the periodic phonon mirror used as seed (empty circles).

though the edges have been slightly rounded. As already mentioned, the width of the stop band depends on the acoustic impedance mismatch between the materials used and the thickness ratio. To change this width, it is possible either to change materials (e.g., using $Al_xGa_{1-x}As$ alloys) or to change the relative thicknesses of the two layers in the period of the seed SL.[4] Using the second option, the design of a second phononic notch filter was performed obtaining a smaller high-reflectivity band. First, we selected the layer thicknesses of a periodic SL that has the desired stop-band width.[4] Afterwards, this structure was used as seed in an optimization process, with the goal of eliminating all the oscillations above and below the stop band. Figure 4 shows the reflectivity curve for an optimized nanowave notch filter. The reflectivity of a periodic (0.55λ,0.45λ) phonon Bragg mirror is also included. The latter has a width reduced to ~30% of the first notch filter. In the bottom panel, the thickness distributions for the periodic structure with a narrow stop band and the optimized version are shown. Again, the steepness in the stop band is slightly affected by the optimization process. A high-reflectivity region of ~0.32 cm^{-1} wide was obtained. With the exception of small features at the edges of the high-reflectivity zone, all oscillations have been completely removed. The steepness in the stop-band edges is affected by the optimization process. It can be seen that important deviations in the thicknesses from the periodic mirror are present in the whole structure.

The NM optimization method, in general, reaches a minimum within or nearby the initial simplex volume. Due to the characteristics of the reflectivity function, there are several minima and multiple feasible solutions. Notwithstanding this fact, there are some target reflectivities where the use of a seed is required to avoid falling in local minima that do not meet the condition stated in Eq. (2) or to significantly accelerate the optimization process.

In what follows, we analyze two devices where the selection of a seed requires a preliminary optimization process.

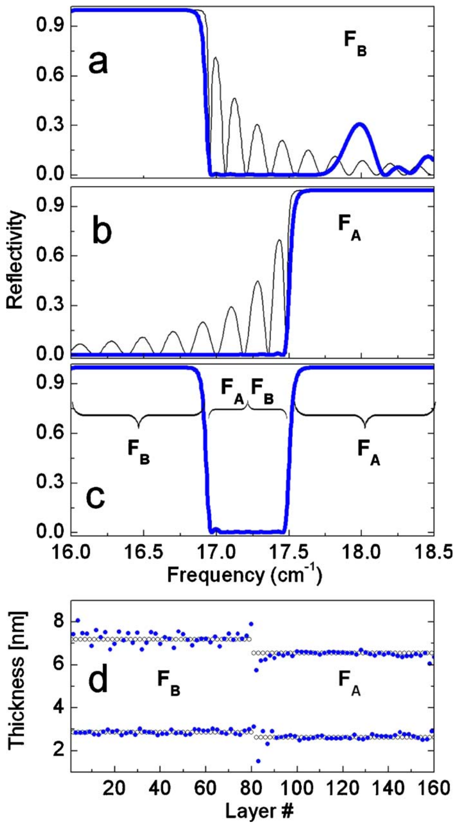

FIG. 5. (Color online) Design of a phononic color filter. (A) Acoustic reflectivity of a first optimized edge filter F_B. The reflectivity of the selected seed is also shown (thin line). (B) Acoustic reflectivity of a first optimized edge filter F_A and the corresponding reflectivity of the periodic seed. (C) Calculated acoustic reflectivity for a color filter made with 160 GaAs/AlAs layers. (D) Layer thicknesses corresponding to the optimized color filter (full dots) and the corresponding periodic phonon mirror (empty circles).

The first complex device is a color filter. Color filters are devices with characteristics of selective transmittance, capable of passing a certain part of the spectrum while being highly reflective to the other portions. They are basically the opposite to a notch filter. Figure 5(c) shows the calculated phonon reflectivity and corresponding layer thicknesses for an optimized 160 layer GaAs/AlAs structure [shown in Fig. 5(d)]. The transmission band was set in the 16.95–17.45 cm^{-1} region. The design of the optimized color filter was performed in a two step optimization process.[1] The first step consisted of two optimizations: a periodic 80 layer GaAs/AlAs 6.56/2.61 nm SL was used as a seed to obtain a filter F_A [Fig. 5(b)], the same as in the case of the basic edge filter. A second periodic 80 layer GaAs/AlAs 7.19/2.85 nm SL was used as a seed to obtain a filter F_B [Fig. 5(a)]. F_B was optimized to have a high transmittance region in the desired band, but a high-reflectivity band between 15.98 and 16.85 cm^{-1}. For comparison purposes, the reflectivity of the associated periodic mirrors is also shown. The optimized color filter is then a 160 layer structure formed by the concatenation of F_B+F_A. A second optimization stage can be implemented to refine details that arise from the coupling of

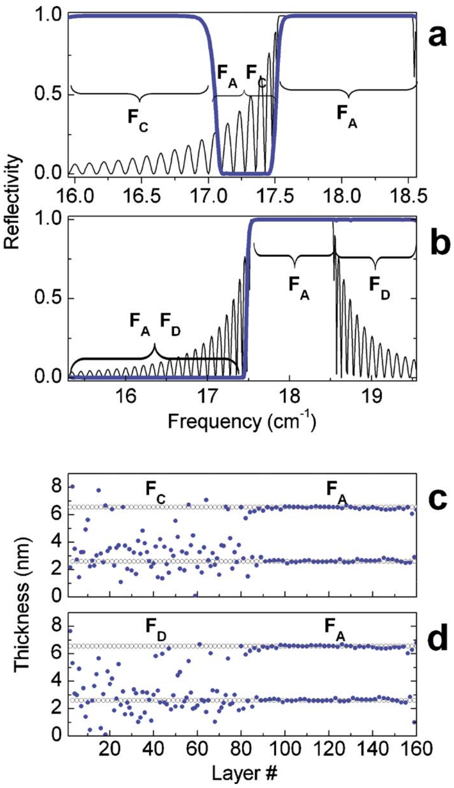

FIG. 6. (Color online) Calculated acoustic reflectivity for (a) an optimized color filter and (b) an optimized edge filter made with 160 GaAs/AlAs layers (thick line). For comparison purposes, the reflectivity of a periodic array is also shown (thin line). (c) and (d) show the layer thicknesses corresponding to the optimized color filter and edge filter, respectively (full dots). The corresponding periodic phonon mirror thicknesses (empty circles) are also shown.

the two initial filters. In this particular device, we have not performed such optimization.

To illustrate the diversity of feasible solutions, we generate a similar color filter, changing the initial seed. We designed a second filter F_C with similar requirements to those imposed on F_B. In the first stage of the optimization, to generate F_C, we used no seed, i.e., all vertices in the simplex were random structures. The second step consisted in the optimization of the desired color filter using the F_C+F_A 160 layer structure as seed. In Fig. 6(a), we show the reflectivity curve of the optimized device along with the corresponding 160 layer periodic SL. In Fig. 6(c), the thickness distribution of the optimized color filter and the periodic mirror are shown. The highly disordered region corresponds to the part of the sample related to the random based filter F_C. Using the outlined optimization scheme, it is easy to fix the transmission region in the color filter, just setting the positions of the individual seed filters F_A and F_C (or F_A and F_B).

The last designed sample is an extended edge filter (edge filter from now on), shown also in Fig. 6, where the target reflectivity curve presents a high-reflectivity region twice wider than that corresponding to the periodic superlattice. It can be seen that the target reflectivity is excellently well reproduced. The design of the optimized edge filter was performed in a two step optimization process.[1] The first step consisted of two optimizations: a periodic 80 layer GaAs/AlAs 6.56/2.61 nm SL was used as a seed to obtain two different filters F_A and F_D. While F_A is the same filter analyzed in the basic edge filter, F_D was meant to have the same high-transmittance region, but to meet the high reflectivity condition in the 18.5–19.5 cm^{-1} band [see Fig. 6(b)]. As in the case of F_A, to optimize F_D, it could also be possible to use random structures, or another seed, with the minigap located in the desired high-reflectivity region. The second step consisted in the optimization of the desired edge filter using the F_D+F_A 160 layer structure as a seed. In Fig. 6(d), the thickness distribution of the optimized edge filter (full dots) and the corresponding periodic structure (empty circles) are shown. Note how the more intense deviations from the periodic case are in the F_D related part of the sample, suggesting that the target reflectivity does not have an associated real structure "near" the chosen periodic seed. The last optimization step is just a refining stage, and minor variations where introduced in the distribution of the filters F_A and F_D. The relevance of this last optimization depends principally on how well designed are the seeds F_D and F_A.

Though in all the presented devices the target reflectivities are excellently reproduced, it must be noted that some arbitrary reflectivity curves cannot be achieved even with the use of *ad hoc* seeds during the optimization process.[29] The steepness of the stop bands and the cavity mode widths, for example, are limited by the number of layers considered in the structure.

In what follows, we will focus our attention on the experimental characterization of three devices described in this section: the broadband mirror (Fig. 1), the color filter, and the edge filter (both corresponding to Fig. 6).

III. CHARACTERIZATION OF THE SAMPLES

We selected three samples to grow and characterize: the broadband mirror, the color filter, and the edge filter. The samples were grown on (001) GaAs substrates using MBE. High resolution x-ray diffraction (HRXRD) and photoluminescence (PL) were used as structural probes of the GaAs/AlAs nonperiodic multilayer structures.

A. High resolution x-ray diffraction

Previous studies of nonperiodic structures were performed using HRXRD, in particular, on Fibonacci arrays and random SLs, showing the usefulness of this technique even in samples where the Bloch theorem is not valid.[14,16–18] A θ-2θ HRXRD scan of the three studied devices using the Cu $K\alpha 1$ radiation is shown in Fig. 7. Both experimental (thick black lines) and simulated curves (thin red lines) are shown for the color filter (top), the edge filter (center), and the broadband mirror (bottom).

Despite of the complexity of the layer thickness distributions in the studied devices (shown in Figs. 1 and 6), some peaks can be directly assigned in the diffractograms. In both the edge filter and the color filter diffractograms, several satellite peaks can be distinguished (labeled by arrows in Fig. 7). The positions of these regular satellite peaks correspond

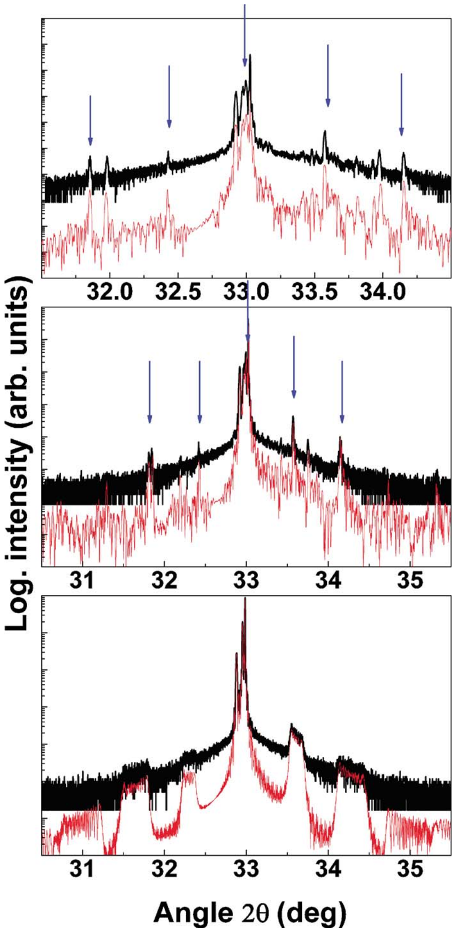

FIG. 7. (Color online) High resolution x-ray data in black (thick) lines and calculated diffraction profile in red (thin) lines for the three studied phononic devices: color filter (top), edge filter (center), and broadband mirror (bottom).

to a periodicity of 9.2 nm (±0.1 nm). It means that these peaks come from the most regular part of the samples (F_A). In the case of the broadband mirror, besides the substrate peak, four satellite square features can be seen. They can be associated with the characteristic peaks present in a periodic SL, and broadened because of the gradient in the layer thicknesses. The general agreement is excellent between the experimental results and the simulations for the three nanowave devices using the nominal values for the layer thicknesses. We have verified that rigid shifts of the thicknesses did not improve the agreement between experiments and simulations. Although previous studies reflect that many of the diffraction patterns are largely unaffected by even substantial amounts of random disorder, HRXRD still represents an important tool for a basic structural characterization of the samples.

B. Photoluminescence

Photoluminescence provides additional information to that obtained from x-ray diffraction studies by probing the electronic levels, which are determined by the confinement in the GaAs layers. This characteristic can be used, in principle, to determine the layer thicknesses. In this section, we present the results of PL experiments and simulations that provide information to identify and characterize the optimized nonperiodic phonon devices.

PL can be used as a rapid characterization technique on this kind of samples. In our case, PL experiments were performed at 80 K using a triple T64000 Jobin-Yvon Raman spectrometer equipped with a liquid-N_2-cooled charge coupled device (CCD), using as excitation the 514.5 nm line of an Ar-Kr laser.

To simulate the photoluminescence process in the phononic devices, we considered the sum of the emissions of individual GaAs quantum wells, each one contributing an emission that was modeled as a Gaussian distribution centered in the calculated fundamental gap energy E_0. Two absorption processes in the sample were taken into account: (1) the absorption of the incident light which affects the excitation of each quantum well, and (2) the absorption of the photoluminescence signal emitted by each quantum well. We neglect the emission following this absorption. Both processes were introduced in the simulation as exponential decaying factors, setting that the light emitted by a specific quantum well (QW) could only be absorbed by thicker QWs present between the emitting QW and the surface of the sample. E_0 for each QW was computed using the transfer matrix method, modeling each QW by an effective finite SL with infinite potential barriers as boundary conditions at both ends of the structure. The program performs a scan in energy until it reaches a value for which the wave function fulfills the boundary conditions. For heavy holes, we used parabolic bands, and for Gamma electrons, the nonparabolicity was described by a two-band envelop function model. The band potential was taken as $E_g = 1519$ meV for GaAs and 2577 meV for AlAs. The effective masses (in units of free electron mass) used were $m_{\Gamma\text{-GaAs}} = 0.067$, $m_{\Gamma\text{-AlAs}} = 0.130$, $m_{hh\text{-GaAs}} = 0.38$, and $m_{hh\text{-AlAs}} = 0.70$; the dielectric constant used was 12.83.

The three aperiodic devices present a different PL spectrum, and the main characteristics compare quite nicely with the simulations. As examples, in Fig. 8 we present the measured (upper panels) and simulated (bottom panels) PL spectra for the edge filter (left) and the broadband mirror (right). The peak present at 825 nm (labeled with an asterisk) corresponds to the bulk GaAs substrate. By comparing the experimental results with the simulations, it is possible to identify the contributions to the complex PL spectra. The broadband mirror presents the simplest structure of the three studied devices: a constant varying distribution of layer thicknesses. This variation produces a broadening of a single PL peak centered at 765 nm. The higher energy luminescence processes are produced in the inner parts of the sample, so the inner QWs are less efficiently excited, and the emission is absorbed all the way back until the photons reach the sample surface. This is reflected as a strong asymmetry of the peak. The simulation reproduces quite well both the position and the shape of the peak. It must be noted that the PL model does not include re-emission processes and, more importantly, the thermalization within and among quantum wells, which falls beyond the scope of this work. These processes

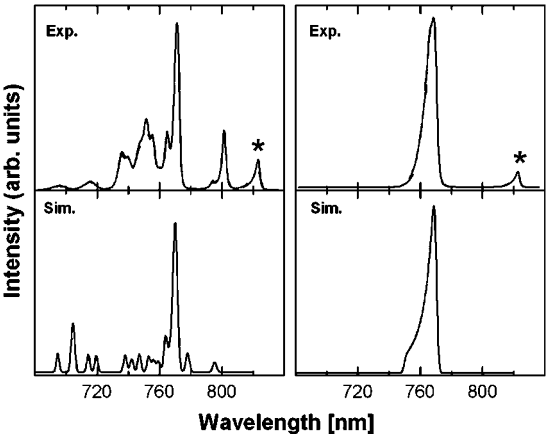

FIG. 8. Measured (upper) and simulated (bottom) photoluminescence spectra for the edge filter (left) and broadband mirror (right). The simulated spectra consider no thermal relaxation. The asterisk labels the GaAs substrate emission.

are very complicated to include in a realistic simulation, posing a strong limitation in the use of PL to fully characterize the structural properties of the samples.

We have characterized the three grown samples, obtaining good agreement between experiments and simulations. These results, together with the HRXRD, allow us to use the nominal thickness values in the following simulations. In the next section, we will focus on the Raman scattering vibrational study of the phononic devices.

IV. RAMAN SCATTERING AND THE INVERSE PROBLEM

Contrary to the field of optics, where light sources and detectors allow the characterization of filters and mirrors, in the terahertz phonon frequency range there are still no acoustic sources and detectors with the required tunability and resolution. Previous studies demonstrate that Raman scattering represents a powerful tool to study the acoustic phonon spectra of periodic,[4] quasiperiodic, and nonperiodic superlattices.[1,12,14,20] In nonperiodic samples, the Raman spectra display a complex series of peaks in the acoustic phonon energy region. Such rich spectra are a kind of sample fingerprint that can be used as a characterization tool.[1] The Raman spectra could be used, in addition, to solve the inverse problem, that is, to derive the layer thicknesses from the Raman data. An implementation of the NM algorithm with multiple objective functions and the nominal structure as initial seed would be a potential tool to characterize the phononic devices directly through their acoustic properties. In this work, we analyze two experimental geometries, namely, backscattering (BS, $k_S \sim -k_L$, $q = \sim 2k_L$) and forward scattering (FS, $k_S \sim k_L$, $q \sim 0$). Here, k refers either to the scattered (S) or laser (L) wave number, and q is the transferred wave number.

In order to evaluate Raman cross sections by acoustic excitations, typically a photoelastic model is used. The expression for the Raman efficiency for a one-dimensional system is given by

$$\sigma(\omega) \propto \frac{1}{\omega}\left[n(\omega) + \frac{1}{2} \pm \frac{1}{2}\right]\left|\int dz E_L(z) E_S^*(z) p(z) \frac{\partial u(z)}{\partial z}\right|^2, \tag{3}$$

where $n(\omega)$ is the Bose-Einstein statistical factor, $p(z)$ is the material dependent photoelastic constant, $u(z)$ is the atomic displacement within the structure, and E_L and E_S are the incident and scattered electric fields, respectively. The phonon displacements are obtained using a matrix method implementation of a continuum theory that includes zero-strain boundary conditions at the sample-air interface.[1,35] Complex values for the photoelastic constant of GaAs and AlAs valid at 514.5 nm are used.[38,39] Absorption is included through the bulk materials' complex index of refraction for the light wavelength used.

Due to absorption effects, from Eq. (3) it can be inferred that the main contribution for the spectra taken under BS configuration is from the layers that are near the excitation surface. On the contrary, in a FS geometry, Eq. (3) becomes

$$\sigma(\omega) \propto e^{-\alpha D}\left|\int dz p(z) \frac{\partial u_w(z)}{\partial z}\right|^2, \tag{4}$$

where D is the total thickness of the sample. Thus, the absorption attenuates the signal in exactly the same way for every layer in the sample and so a FS spectrum has information about the whole structure. It is clear that the FS spectra provide not only additional but also complementary information to that accessible in a BS geometry, reflecting the importance of the different studied geometries.

In order to illustrate the problem of inverse engineering, i.e., to determine the layer thicknesses of a structure given the experimental Raman spectra, we will analyze the case of the color filter introduced in Sec. II (Fig. 6(a), 160 layers). To simplify the problem, we will consider only two parameters: a variation of the layer thicknesses between 0.90 and 1.10 of the nominal value for each material (GaAs and AlAs). After the conception, design, and optimization of the color filter, we obtain a nominal thicknesses distribution [Fig. 6(c)]. To continue with our example, suppose that such a sample is grown by MBE, and all the GaAs layer thicknesses are reduced by 2% and all the AlAs layer thicknesses are increased by 1%. In our gedanken experiment, we perform Raman scattering from different geometries and compare the spectra with simulations. The task is to find the point (0.98, 1.01) by comparing Raman spectra simulations using different GaAs/AlAs layer thicknesses with the measured spectra.

In Fig. 9, we plot the objective function as a function of the two parameters. Two experimental resolutions were simulated, σ=0.01 cm^{-1} (left side panels), corresponding to an ultrahigh resolution Raman setup, and σ=0.20 cm^{-1} (right side panels), reachable with a triple spectrometer as the one described in the next section. Typical Raman spectra are illustrated in Figs. 10–12. Top (center) panels illustrate the use of a BS (FS) spectrum as a target, while bottom panels use both the BS and FS spectra (BS+FS case). The white cross indicates the absolute minimum location. It is worthwhile to note that the topology is smoother in the BS+FS case, and the absolute minimum better defined. By decreas-

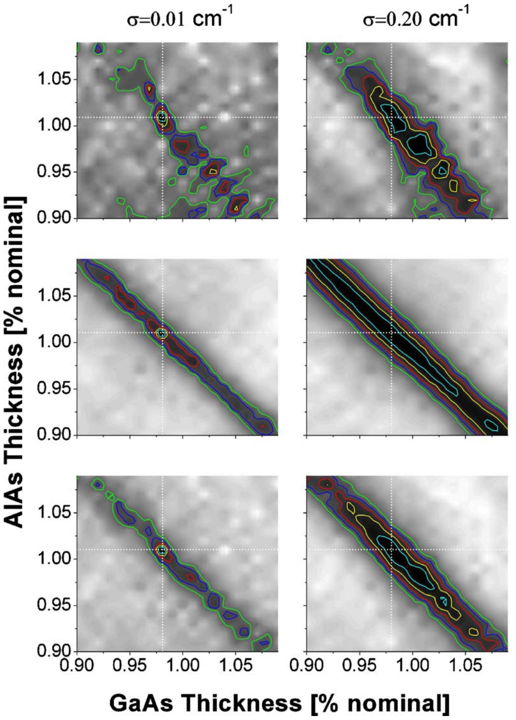

FIG. 9. (Color online) Color filter objective function evaluated for structures with layers modified by a constant factor between 0.9 and 1.1 for each constituent material. Two experimental resolutions were simulated: σ=0.01 cm^{-1} (left side panels) and σ=0.20 cm^{-1} (right side panels). Top (center) panels illustrate the use of a BS (FS) spectrum as a target, while bottom panels use both the BS and FS spectra. The white cross indicates the absolute minimum location.

ing the working resolution, all the parameter space is "flattened," and minima spaces are broader and more extended. For the six cases, absorption was considered through the bulk materials' complex index of refraction for a 514.5 nm wavelength.

The efficient solution of the inverse problem, i.e., the determination of the actual thickness distribution from the results of a Raman scattering experiment, must deal at least with two basic problems: the uniqueness of the solution and the development of a reliable model of the Raman scattering process. From a theoretical point of view, a broadband Raman scattering complex signal would provide enough information to solve the inverse problem. However, in real Raman scattering experiments, what is measured is an intensity over a reduced spectral band. There are multiple solutions that give practically the same Raman spectrum in a particular spectral window. In addition, the strong light absorption in the samples, which are thicker than 300 nm, limits the layers that are probed in a BS Raman experiment excited with visible light. The main contribution for the spectra taken under the BS configuration is from the layers that are near the excitation surface within the penetration depth (typically ~55 nm at 514.5 nm for bulk GaAs). The use of near infrared excitation, for which the penetration depth is larger, is limited due to the related small Raman intensities. Using only one BS spectrum for such a complex inverse problem leads to multiple feasible solutions (see top panels in Fig. 9). The use of additional excitation lines provides an increasing number of constraints that would limit the number of feasible solutions. Nevertheless, all these additional constraints have a limited contribution from the inner layers, thus only providing complementary information about the first layers. An alternative way to reduce the solution space is through the use of alternative geometries. In this work, we study two possible solutions: to perform BS from the backside of the samples, the contribution of the substrate side layers being the most important; and FS, where absorption effects affect all the layers in the same way. The determination of the real structure, using both the BS and FS spectra, represents a possibility toward the definition of a well posed inverse problem. The increase of the working resolution uncovers details in the spectra that help to reduce the minima area in the parameter space (compare the minima for the two considered resolutions in Fig. 9). High resolution Raman setups working in the visible region can discern spectral features with resolution better than 0.02 cm^{-1},[40] allowing us to probe the required details in the spectra. The second point in order to solve the inverse problem is the selection of the model. The photoelastic model may not be valid close to electronic

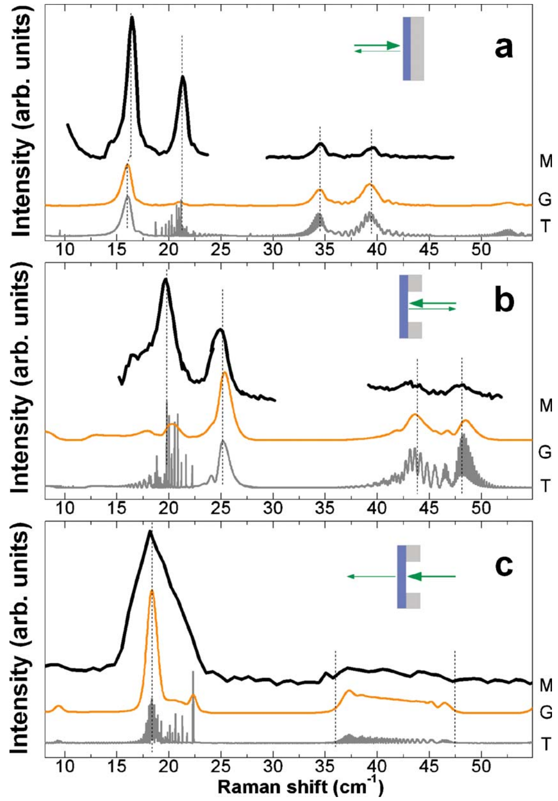

FIG. 10. (Color online) Raman spectra of the broadband mirror using different geometries: (a) and (b) correspond to backscattering Raman spectra taken from different sides of the sample (see text for details), while (c) corresponds to forward Raman scattering. T, G, and M indicate the simulated spectra using a photoelastic model, the simulation Gaussian convoluted to take into account the experimental resolution, and the measured Raman spectra in additive mode, respectively.

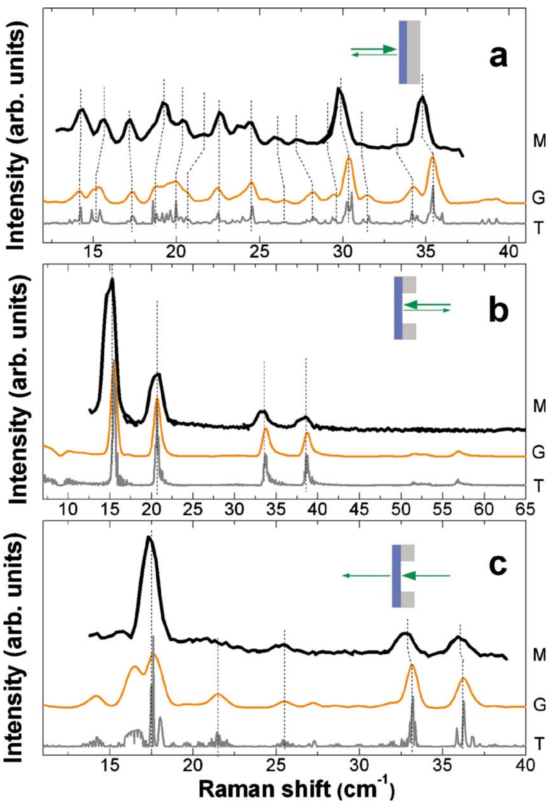

FIG. 11. (Color online) Same as Fig. 10, but for the color filter.

resonances, and it is well known that the photoelastic constants strongly depend on energy. In addition, recent studies demonstrate that taking a constant value within each layer is not a good approximation to match the peak intensities.[41,42] It is clear that new developments in these lines are required.

In this section, we have illustrated what is the motivation for the use of Raman scattering in the solution of the inverse problem, and what are the present experimental and theoretical limitations that require further research and development. In the next section, we present the results on Raman scattering experiments and simulations, using different geometries and a resolution of 0.4 cm^{-1}, where information about the acoustic excitations can be directly obtained.

V. RAMAN SCATTERING CHARACTERIZATION OF PHONONIC DEVICES

We performed Raman scattering experiments on the three grown samples in three different geometries: FS, and BS from the sample and from the substrate sides. The experiments were performed at room temperature using the 514.5 nm line of an Ar-Kr ion laser. The collected spectra were dispersed using a triple T64000 Jobin-Yvon Raman spectrometer equipped with a liquid N_2 CCD in the subtractive (1.2 cm^{-1}) and additive (typical resolution of 0.4 cm^{-1}) modes. The spectra were modeled on the basis of a photoelastic interaction [see Eq. (3)].[1,4,35] Published data of the photoelastic constants, sound speed, and density values for GaAs and AlAs were used.[38,39]

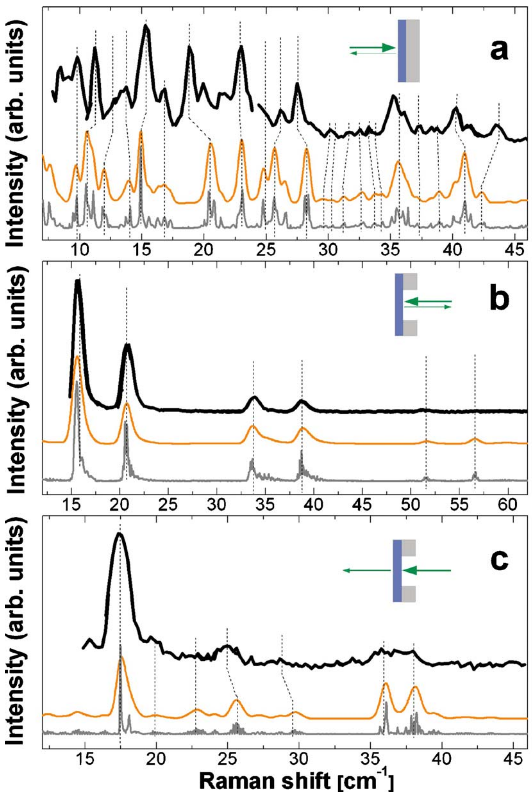

FIG. 12. (Color online) Same as Fig. 10, but for the edge filter.

To perform the Raman scattering experiments in FS and BS from the backside of the samples, it is necessary to remove the GaAs substrate. The preparation of the samples for these experiments was first done by mechanically thinning the substrate to a thickness of approximately 70–130 μm. The sample was then mounted on a sapphire crystal with cyanoacrylate glue. The area thinned was approximately 9 mm^2. The remaining substrate was then selectively chemically etched. The etching solution was a mixture of 30% concentrated hydrogen peroxide (H_2O_2) and 30% concentrated ammonium hydroxide (NH_4OH).[36,37] The composition of the solution was 60:1 and it was held at 0 °C using an ice bath to keep it from overheating. The chemical etching stops in the first few layers of AlAs, leaving a smooth surface and the sample almost unaltered.

Figure 10 shows both the calculated (T) and the measured (M) Raman scattering spectra of the broadband mirror sample in additive mode. A Gaussian convolution of the calculated curve (G) is also included to take into account the finite experimental resolution. Figure 10(a) [Fig. 10(b)] corresponds to the BS spectra measured from the sample (substrate) side. A possible assignment of the peak positions is indicated with dashed lines. Due to light absorption, the BS spectra are very similar to the ones obtained with standard periodic SLs, i.e., a series of doublets near the Brillouin zone center. The broadband mirror has a constant gradient in the layer thicknesses; thus, the BS Raman spectrum from the substrate side should be very similar to the one taken from the sample side, but with a clear shift in the position of the peaks, reflecting the variation in the layer widths. The determination of the peak shifts gives a direct clue on possible differences between the nominal and actual values of adjustment parameters (sound velocities, thicknesses, etc.). By comparing the spectra taken from the two sides, a clear shift of approximately 5 cm^{-1} can be observed, in accordance with the nominal gradient introduced in the sample. It must be noted that a few periods on the substrate side could have been removed by the chemical etching, hiding some possible thickness shifts. Figure 10(c) shows the Raman spectrum taken in a forward scattering configuration. In this case, the spectrum gives information in a simple way: in the region around 19 cm^{-1}, one broad peak can be seen, while an almost constant signal is observed in the 35–45 cm^{-1} region. The constant signal gives evidence of the variation in the layer thicknesses, similar to the results obtained with x-ray diffraction. Note the overall very good agreement between the measured and calculated data. There are, however, some clear details in which differences are observed. For example, note Fig. 10(a) the calculated smaller relative amplitude of the 20 cm^{-1} peak.

Figure 11 shows the Raman spectra corresponding to the color filter. Figure 11(a) shows quite good agreement, although not perfect between the measurements (M) and the simulations (G). The spectrum presents a very rich spectrum where many peaks can be observed, in contrast with the spectra corresponding to the broadband mirror. Curve T shows that some higher resolution details remain hidden. As indicated in Sec. II, the backside of the sample is dominated by an almost periodic array of layers, coming from the optimization of F_A. Due to the limited working resolution of the spectrometer and the regularity of this side of the sample, we expect to have basically the spectra of a periodic SL with high resolution features originated by the small departure from periodicity. In the spectra shown in Fig. 11(b), up to 3 orders of the folded phonons can be distinguished. Note the contrast with the BS spectra shown in the upper panel, where no SL doublets can be identified. The intense peak at ~ 18 cm^{-1} in Fig. 11(c) is related to the regular part of the sample, while the rest of the features correspond to the ensemble of layers. Though an excellent agreement has been reached, some differences in the relative intensities can still be noted. The latter spectrum has information on the whole structure; nevertheless, the BS spectra taken from the sample side present a richer structure of peaks that could be more sensitive to changes in the layer thickness from the disordered part of the sample.

The last measured sample is the edge filter. The Raman spectra are shown in Fig. 12. For this structure, the calculations reproduce almost every detail of the measured spectra, and the relative intensities match quite well. Note once again the difference between the sample side BS Raman spectrum and those corresponding to the other samples. As in the case of the color filter, the substrate side BS Raman spectrum presents a series of doublets related to the quasiperiodic half of the sample. It is evident from the spectra of the edge and color filters the strong effects of the light absorption: the BS Raman spectra from different sides of the sample are completely different. A strong peak in the FS spectrum can be related to the almost periodic half of the sample.

VI. DISCUSSION AND CONCLUSIONS

In this paper, we have shown that it is possible to extend concepts from optics to phononics in the gigahertz to terahertz range to design passive devices as, e.g., filter and mirrors. In addition, we have shown that optimization tools used in other domains can be implemented for the design of these devices. As follows from our experience, the best way to exploit these procedures is to start with intelligent seeds and to optimize them, using, for example, a NM based routine. Dealing with phononic devices in the terahertz range poses a series of challenges for their implementation in technological applications. Firstly, one of the main challenges is the selection of materials with appropriate acoustic properties. Secondly, for their implementation as terahertz devices (i.e., in the nanometer wavelength), it is required that they can be grown with very high thickness control and atomically flat interfaces. This implies that epitaxial techniques are a requirement. A growing technique like MBE imposes strong limitations over the number of materials that can be grown. Because of the lattice mismatch, the number of useful materials for aperiodic phononic devices is, in addition, reduced. Up to now, besides GaAs/AlAs multilayers, several materials have been successfully grown using MBE, e.g., group III-V semiconductors (GaAlAs alloys, GaInAs, AlInAs, GaP, GaN, AlN, GaMnAs, etc.), group IV semiconductors (Si, Ge, and SiGe alloys), group II-VI semiconductors (CdTe, MgTe, and ZnSe), and several oxide materials such as $\mathrm{SrTiO_3}$ and $\mathrm{BaTiO_3}$. However, each pair of materials requires specific consideration at the moment of designing an aperiodic multilayer for phononic applications. For example, $\mathrm{SrTiO_3}$ and $\mathrm{BaTiO_3}$ have to be grown in an integer and limited number of monolayers. GaAs/AlAs represents one of the simplest cases, because of the low lattice mismatch. Finally, an important feature that differentiates optics and hyperacoustics in the terahertz range is the characterization of samples. In fact, the access to spectral and time domain probes with sufficient resolution to test hyperacoustic multilayered devices represents today an open problem.

The electronic characterization of the samples, through PL, is only qualitative mainly due to the limitations in the simulations related to thermalization, both within the wells and between the wells. On the contrary, the results of HRXRD allowed us to use the nominal values in the simulations of Raman scattering. The agreement between model and experimental Raman spectra is quite good, confirming the hypothesis that it is a good acoustic characterization tool for acoustic nanowave devices in the terahertz range. Available ultrahigh resolution setups along with more accurate models and material parameters can directly be used as a spectral-domain tool able to probe the high resolution details of the phononic devices. The development of sound transducers, sources, detectors, and new techniques capable of working in this energy range[11,43,44] would provide a new means to probe the described optimized passive devices.

We have been initially motivated to use Raman scattering as a means to solve the inverse problem, proposing the use of different geometries to reduce the solution space. An alternative is to use different excitation energies with different absorption coefficients in a BS geometry or to use near infrared where the absorption is small. Note, however, that we were unable to perform experiments in the near infrared due to low Raman signal and high PL intensities. We observed that there are subtle differences in peak intensities and positions between theory and experiments, which could come from the fact of considering a constant photoelastic factor in each layer and the omission of electronic resonances with the excitation wavelength. The use of available bulk material parameters could also contribute to these differences. All of these require further work in the development of a Raman scattering model and on the determination of reliable material parameters. The development of nanophononics should represent a new motivation to accomplish these goals.

A structure with arbitrary layer sequence could be designed to act as a tailored phonon source in pump-probe experiments. The design and optimization not only of passive devices (filters and mirrors, like the ones studied in this work) but also of active devices like sources with a predetermined energy spectrum would be an interesting development.

In conclusion, we have extended concepts previously discussed in the context of photonics to the physics of acoustic phonons, designing and growing nonperiodic nanowave devices. We have described in detail the design and characterization of three semiconductor phononic devices capable of controlling terahertz acoustic phonons. We have also shown that Raman scattering is an excellent probe of the acoustic excitations in the spectral domain. In this work, we have observed that the BS geometry provides reliable information about the layers next to the excitation side, and the FS spectrum complements this information since it is formed by contributions from all layers identically attenuated. The described tools represent the starting point for the conception of new complex passive and active phononic devices in the technologically relevant terahertz range.

ACKNOWLEDGMENTS

The authors acknowledge R. Teissier for the code of energy level calculations in heterostructures. This work is supported by a SECyT-ECOS(Sud) collaboration. N.D.L.K. acknowledges support from Fundación YPF (Argentina). A.F. also acknowledges support from ANPCyT through Grant No. PICT2004 25316, and from the ONR (U.S.).

---

*kimura@cab.cnea.gov.ar
†afains@cab.cnea.gov.ar

[1] N. D. Lanzillotti-Kimura, A. Fainstein, A. Lemaître, and B. Jusserand, Appl. Phys. Lett. **88**, 083113 (2006).

[2] A. A. Balandin, J. Nanosci. Nanotechnol. **5**, 1 (2005).

[3] V. Narayanamurti, H. L. Störmer, M. A. Chin, A. C. Gossard, and W. Wiegmann, Phys. Rev. Lett. **43**, 2012 (1979).

[4] B. Jusserand and M. Cardona, in *Light Scattering in Solids*, edited by M. Cardona and G. Güntherodt (Springer, Heidelberg, 1989), Vol. V, p. 49.

[5] P. Lacharmoise, A. Fainstein, B. Jusserand, and V. Thierry-Mieg, Appl. Phys. Lett. **84**, 3274 (2004).

[6] A. Soukiassian, W. Tian, D. A. Tenne, X. X. Xi, D. G. Schlom, N. D. Lanzillotti-Kimura, A. Bruchhausen, A. Fainstein, H. P. Sun, Xiaoqing Pan, A. Cross, and A. Cantarero, Appl. Phys. Lett. **90**, 042909 (2007).

[7] S. Mizuno and S. I. Tamura, Phys. Rev. B **45**, 734 (1992).

[8] S. I. Tamura, H. Watanabe, and T. Kawasaki, Phys. Rev. B **72**, 165306 (2005).

[9] M. Trigo, A. Bruchhausen, A. Fainstein, B. Jusserand, and V. Thierry-Mieg, Phys. Rev. Lett. **89**, 227402 (2002); see also J. M. Worlock and M. L. Roukes, Nature (London) **421**, 802 (2003).

[10] A. Huynh, N. D. Lanzillotti-Kimura, B. Jusserand, B. Perrin, A. Fainstein, M. F. Pascual-Winter, E. Perónne, and A. Lemaître, Phys. Rev. Lett. **97**, 115502 (2006).

[11] Kung-Hsuan Lin, Chieh-Feng Chang, Chang-Chi Pan, Jen-Inn Chyi, Stacia Keller, Umesh Mishra, Steven P. DenBaars, and Chi-Kuang Sun, Appl. Phys. Lett. **89**, 143103 (2006).

[12] N. D. Lanzillotti-Kimura, A. Fainstein, C. A. Balseiro, and B. Jusserand, Phys. Rev. B **75**, 024301 (2007).

[13] Helios Sanchis-Alepuz, Yuriy A. Kosevich, and Jose Sanchez-Dehesa, Phys. Rev. Lett. **98**, 134301 (2007).

[14] R. Merlin, in *Light Scattering in Solids*, edited by M. Cardona and G. Güntherodt (Springer, Heidelberg, 1989), Vol. V, p. 214, and references therein.

[15] S. Tamura and J. P. Wolfe, Phys. Rev. B **36**, 3491 (1987).

[16] R. Merlin, IEEE J. Quantum Electron. **24**, 3491 (1988).

[17] R. Merlin, K. Bajema, R. Clarke, F.-Y. Juang, and P. K. Bhattacharya, Phys. Rev. Lett. **55**, 1768 (1985).

[18] A. T. Macrander, G. P. Schwartz, and J. Bevk, Phys. Rev. B **37**, 8459 (1988).

[19] A. Sasaki, Thin Solid Films **306**, 346 (1997).

[20] B. Jusserand, D. Paquet, F. Mollot, M. C. Joncour, and B. Etienne, Phys. Rev. B **39**, 3683 (1989).

[21] A. Khelif, A. Choujaa, B. Djafari-Rouhani, M. Wilm, S. Ballandras, and V. Laude, Phys. Rev. B **68**, 214301 (2003).

[22] R. Sainidou, B. Djafari-Rouhani, Y. Pennec, and J. O. Vasseur, Phys. Rev. B **73**, 024302 (2006).

[23] F. Cervera, L. Sanchis, J. V. Sanchez-Perez, R. Martinez-Sala, C. Rubio, F. Meseguer, C. Lopez, D. Caballero and J. Sanchez-Dehesa, Phys. Rev. Lett. **88**, 023902 (2001).

[24] A. Khelif, B. Djafari-Rouhani, J. O. Vasseur, P. A. Deymier, P. Lambin, and L. Dobrzynski, Phys. Rev. B **65**, 174308 (2002).

[25] Y. Pennec, B. Djafari-Rouhani, J. O. Vasseur, H. Larabi, A. Khelif, A. Choujaa, S. Benchabane, and V. Laude, Appl. Phys. Lett. **87**, 261912 (2005).

[26] Y. Pennec, B. Djafari-Rouhani, J. O. Vasseur, A. Khelif, and P. A. Deymier, Phys. Rev. E **69**, 046608 (2004).

[27] P. Baumeister, J. Opt. Soc. Am. **48**, 955 (1958).

[28] D. A. Tenne, A. Bruchhausen, N. D. Lanzillotti-Kimura, A. Fainstein, R. S. Katiyar, A. Cantarero, A. Soukiassian, V. Vaithyanathan, J. H. Haeni, W. Tian, D. G. Schlom, K. J. Choi, D. M. Kim, C.-B. Eom, H. P. Sun, X. Q. Pan, Y. L. Li, L. Q. Chen, Q. X. Jia, N. M. Nakhmanson, K. M. Rabe, and X. X. Xi, Science **313**, 15371 (2006).

[29] D. Bria, B. Djafari-Rhouhani, A. Bousfia, E. H. El Boudouti, and A. Nougaoui, Europhys. Lett. **55**, 841 (2001).

[30] G. Malpuech and A. Kavokin, Semicond. Sci. Technol. **16**, R1 (2001), and references therein.

[31] J. A. Nelder and R. Mead, Comput. J. **7**, 308 (1965).

[32] J. C. Lagarias, J. A. Reeds, M. H. Wright, and P. E. Wright, SIAM J. Optim. **9**, 112 (1998).

[33] Kai-Yew Lum, Pierre-Marie Jacquart, and Mourad Sefrioui, *Constrained Optimization of Multilayered Anti-Reflection Coatings using Genetic Algorithms*, in Proceedings of the Fourth Asia-Pacific Conference on Simulated Evolution and Learning (SEAL '02), edited by Lipo Wang, Kay Chen Tan, Takeshi Furuhashi, Jong-Hwan Kim, and Xin Yao (Nanyang Technical University, Singapore, 2002), Vol. 1, p. 172.

[34] W. H. Press, S. A. Teukolsky, W. T. Vetterling, B. P. Flannery, *Numerical Recipes in C, The Art of Scientific Computing*, 2nd ed. (Cambridge University Press, Cambridge, England, 1992), p. 408.

[35] O. Pilla, V. Lemos, and M. Montagna, Phys. Rev. B **50**, 11845 (1994).

[36] J. J. Lepore, J. Appl. Phys. **51**, 6441 (1980).

[37] R. A. Logan and F. K. Reinhart, J. Appl. Phys. **44**, 4172 (1973).

[38] Z. V. Popovic, J. Spitzer, T. Ruf, M. Cardona, R. Notzel, and K. Ploog, Phys. Rev. B **48**, 1659 (1993).

[39] Sadao Adachi, J. Appl. Phys. **58**, R1 (1985).

[40] A 2 m SOPRA double grating spectrograph can have a resolution of around 0.02 cm^{-1}. A tandem Fabry-Pérot Raman monochromator setup can improve this performance down to 0.005 cm^{-1}. See, e.g., J. P. Pinan, R. Ouillon, P. Ranson, M. Becucci, and S. Califano, J. Chem. Phys. **109**, 5469 (1998).

[41] T. Ruf, J. Spitzer, V. F. Sapega, V. I. Belitsky, M. Cardona, and K. Ploog, Phys. Rev. B **50**, 1792 (1994).

[42] Adnen Mlayah, Jean-Roch Huntzinger, and Nicolas Large, Phys. Rev. B **75**, 245303 (2007).

[43] A. J. Kent, N. M. Stanton, L. J. Challis, and M. Henini, Appl. Phys. Lett. **81**, 3497 (2002).

[44] C. E. Martinez, N. M. Stanton, P. M. Walker, A. J. Kent, S. V. Novkov, and C. T. Foxon, Appl. Phys. Lett. **86**, 221915 (2005).